


Construction Of High Loading Natural Active Substances Nanoplatfom and Application in Synergistic Tumor Therapy

Haoqiang Liu^{1,*}, Zeyidan Jiapaer^{1,*}, Fanxing Meng¹, Wanfeng Wu¹, Chengyi Hou², Mengjiao Duan¹, Yanan Qin¹, Shuxuan Shao¹, Minwei Zhang¹

¹Xinjiang Key Laboratory of Biological Resources and Gentic Engineering, College of Life Science & Technology, Xinjiang University, Urumqi, 830046, People's Republic of China; ²State Key Laboratory for Modification of Chemical Fibers and Polymer Materials, College of Materials Science and Engineering, Donghua University, Shanghai, 201620, People's Republic of China

*These authors contributed equally to this work

Correspondence: Shuxuan Shao; Minwei Zhang, Email Shaoshux@126.com; zhangmw@xju.edu.cn

Background: Natural bioactive substances have been widely studied for their superior anti-tumor activity and low toxicity. However, natural bioactive substances suffer from poor water-solubility and poor stability in the physiological environment. Therefore, to overcome the drawbacks of natural bioactive substances in tumor therapy, there is an urgent need for an ideal nanocarrier to achieve high bioactive substance loading with low toxicity.

Materials and Methods: Face-centered cubic hollow mesoporous Prussian Blue (HMPB) NPs were prepared by stepwise hydrothermal method. Among them, PVP served as a protective agent and HCl served as an etching agent. Firstly, MPB NPs were obtained by 0.01 M HCl etching. Then, the highly uniform dispersed HMPB NPs were obtained by further etching with 1 M HCl.

Results: In this work, we report a pH-responsive therapeutic nanoplatfom based on HMPB NPs. Surprisingly, as-prepared HMPB NPs with ultra-high bioactive substances loading capacity of 329 $\mu\text{g mg}^{-1}$ owing to the large surface area (131.67 $\text{m}^2 \text{g}^{-1}$) and wide internal pore size distribution (1.8–96.2 nm). Moreover, with the outstanding photothermal conversion efficiency of HMPB NPs (30.13%), natural bioactive substances were released in the tumor microenvironment (TME). HMPB@PC B2 achieved excellent synergistic therapeutic effects of photothermal therapy (PTT) and chemotherapy (CT) *in vivo* and *in vitro* without causing any extraneous side effects.

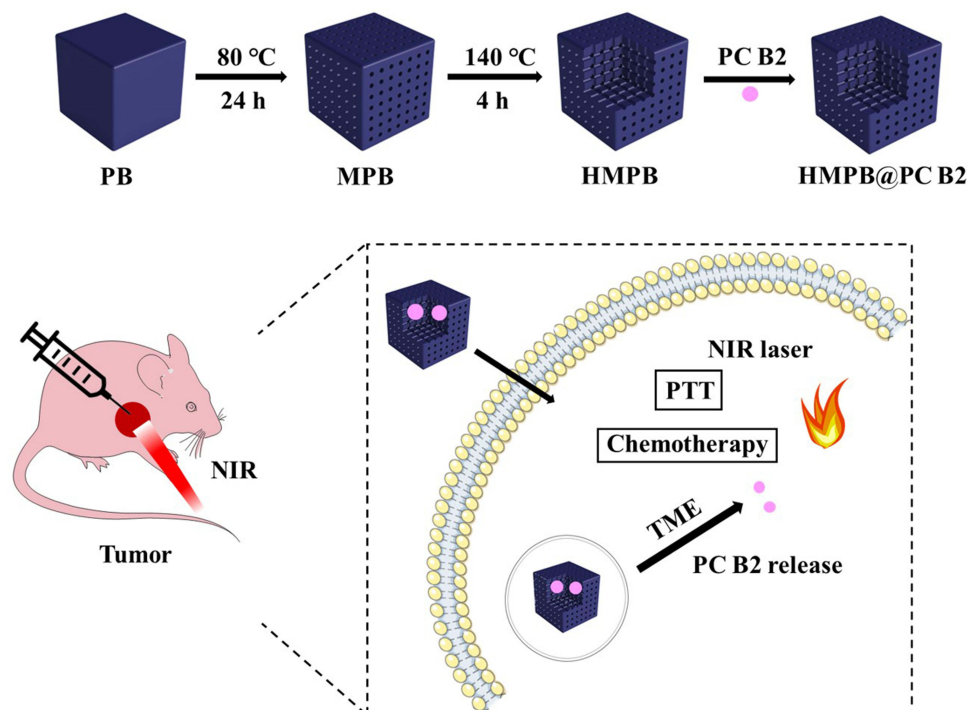
Conclusion: A biocompatible HMPB@PC B2 nanoplatfom was constructed by simple physical adsorption. The *in vitro* and *in vivo* experiment results demonstrated that the synergy of PTT/CT provided excellent therapeutic efficiency for cervical cancer without toxicity. Altogether, as-designed nanomedicines based on natural bioactive substances may provide a promising strategy for cancer therapy.

Keywords: HMPB NPs, natural bioactive substances, synergistic therapy, negligible side effect

Introduction

Many natural bioactive substances, especially polyphenols and flavonoids, inhibit various enzymes involved in cell proliferation and signaling pathways in cancer cells and have good tumor inhibitory effects.^{1,2} Procyanidin B2 (PC B2) is the most common variety procyanidin dimer in nature and has strong biological activity.³ It can inhibit tumor cell growth and induces tumor cell apoptosis, thus effectively treating cancer. At the same time, PC B2 are not significantly toxic to normal cells at high concentrations, making it potent drug for cancer treatment.^{4–6} However, PC B2 suffers from poor stability and low bioavailability in organisms, which has limited its application in biomedicine. Currently, bioactive substances can be physically encapsulated into inorganic materials or organic polymers, thus significantly improving their stability and utilization.⁷ At this stage, the commonly used nanocarriers mainly include microcapsules, liposomes,

Graphical Abstract



proteins, and inorganic materials.^{8–11} Liposomes, one of the first nanocarriers used, still have many challenging problems in loading drugs. The structure of liposomes tends to collapse, causing leakage of drugs. On the other hand, the soft structure makes it difficult to be taken up by cells, resulting in a low release rate of the drug in the cells.^{12,13} Protein has been a novel nanocarrier in recent years.^{14–16} Protein-loaded drugs could target specific tissues and organs to achieve the slow release of drugs. Furthermore, they have excellent biocompatibility.^{17,18} However, the high cost of human-derived protein isolation and extraction makes it challenging to further development.¹⁹ Organic macromolecular polymers are also commonly used as drug carriers and are biodegradable in organisms. However, some polymers have significant cytotoxicity.^{20,21} Therefore, there is an urgent need for an ideal nanocarrier to achieve high bioactive substance loading with low toxicity.

As a common coordination compound, Prussian blue is widely used as a nanocarrier in cancer therapy. It is approved by the US Food and Drug Administration (FDA) as a clinical drug for the antidote of heavy metals and radiotherapy.^{22,23} Moreover, PB-based nanomedicines have excellent stability and biocompatibility *in vivo*. On the other hand, it could extend the blood half-life, displaying good biodistribution and pharmacokinetic properties. Meanwhile, PB-based nanomedicines could be excreted out of the body via glomerular and blood pathways.^{24,25} More importantly, to meet its application in biomedicine, PB NPs can be transformed into HMPB NPs with a metal-organic framework (MOF) structure by controlled chemical etching.^{26–28} Generally, HMPB NPs are widely used as nanocarriers for novel therapeutics because of their high specific surface area, high loading, good stability, and easy surface functionalization.^{29,30} For instance, HMPB NPs are used to deliver doxorubicin into tumor tissue to improve the therapeutic effect and avoid unnecessary drug loss.³¹ More surprisingly, compared with pure PB NPs, HMPB NPs are endowed with a higher molar extinction coefficient and photothermal conversion efficiency due to the unique structure that enhances Near Infrared (NIR) absorption. Therefore, it has great potential to replace conventional nanocarriers.^{32,33}

Herein, we delicately constructed PB bio-nanocomposites loaded with PC B2 to overcome the poor stability and low bioavailability of bioactive substances, which can be used for efficient synergistic therapy PTT and CT. HMPB NPs were

successfully synthesized by the hydrothermal method. Polyvinylpyrrolidone (PVP) and HCl as a protective agent and etching agent, separately.^{34,35} The solid PB NPs were first transformed from mesoporous structures and finally into hollow mesoporous structures with huge internal pores. As-prepared HMPB NPs had ultra-high loading of bioactive substances ($329 \mu\text{g mg}^{-1}$) and excellent photothermal conversion efficiency (30.13%). In this work, we confirmed that the constructed PB bio-nanocomposites can achieve controlled PC B2' release and enhanced therapeutic effects, which are expected to further expand the application of bio-nanocomposites in cancer therapy.

Materials and Methods

Reagents and Materials

All chemicals were of analytical grade and used directly without further purification. Polyvinylpyrrolidone (PVP, K30), potassium ferricyanide ($\text{K}_3[\text{Fe}(\text{CN})_6]$ 98%), and hydrochloric acid (HCl, 36.0%~38.0%) were purchased from the Yongsheng Fine Chemicals Co., LTD (Tianjin, China). PC B2 was purchased from Sunny Biotech Co., LTD (Shanghai, China). 3-(4,5-Dimethylthiazol-2-yl)-2,5-diphenyltetrazolium bromide (MTT) was obtained from Beyotime Biotechnology Co. (Haimen, China). Annexin V-FITC/propidium iodide (PI) apoptosis detection kit was supplied by Yeasen Biotech Co., Ltd. (Shanghai, China). Calcein-AM/PI was purchased from Solarbio Science & Technology Co., LTD (Beijing, China). Phosphate buffer solution (PBS) and RPMI 1640 medium were obtained from GIBCO/Invitrogen Co., LTD (Beijing, China). Fetal bovine serum (FBS) was purchased from Biological Industries Co., LTD (Israel).

Preparation of HMPB NPs

The HMPB NPs were prepared by hydrothermal reaction.³⁵ In detail, first, PVP (3.0 g), $\text{K}_3[\text{Fe}(\text{CN})_6]$ (132 mg), and HCl solution (0.01 M, 40 mL) were mixed under magnetic stirring. After obtaining a clear solution, the solution was heated at 80°C for 24 hours. Then, mesoporous Prussian blue nanoparticles (MPB) were obtained by centrifugation (14,000 rpm, 15 min), and unreacted PVP was removed by repeated washing in a mixture of deionized water and ethanol. PVP (5 mg mL^{-1}) was added to MPB NPs (1 mg mL^{-1}) solution in a Teflon vessel and reacted in the presence of 1 M HCl for three hours. Subsequently, the solution was transferred to 140°C and continued to etch for another 3 hours. After the solution was cooled to room temperature, the precipitate was washed repeatedly in a deionized water and ethanol mixture after centrifugation (14,000 rpm, 15 min) and finally vacuum freeze-dried to obtain HMPB NPs powder.

Assessment of Biodegradability of HMPB NPs

The 1 mg mL^{-1} of HMPB NPs suspension was dispersed in PBS buffer with different pH values (7.2, 5.0) to simulate the artificial physiological environment and the acidic environment of lysosomes.^{35,36} Then, the sample solutions were stirred slowly (37°C , 150 rpm) in a constant temperature culture shaker (150 rpm). Subsequently, the sample solutions were collected at different time intervals, and a UV-visible absorption spectrometer measured the UV-visible absorption spectra of the sample solutions.

Loading and Releasing of PC B2 in HMPB NPs

1 mg mL^{-1} HMPB NPs solution was mixed with an equal volume of PC B2 solution (1 mg mL^{-1}). The two solutions were mixed and left to stir at room temperature overnight. The unbound fraction was removed by centrifugation (14,000 rpm, 15 min) to obtain HMPB@PC B2, and then washed repeatedly with deionized water. The natural bioactive load of the material was also assessed by measuring the UV-visible absorbance of the solution before and after the interaction of PC B2 with HMPB NPs at the characteristic absorption peak of PC B2 (280 nm). PC B2 loading capacity was measured using the following equation:

$$\text{Loading capacity} = \frac{(\text{total PC B2} - \text{unbounded PC B2})}{\text{total HMPB}}$$

To determine the pH-responsive release behavior of HMPB@PC B2, a dialysis method was used to investigate the *in vitro* release behavior. Dialysis bags (MWCO = 3.5 kDa) containing 5 mL of HMPB@PC B2 (1 mg mL^{-1}) were dispersed in 20 mL PBS buffer with different pH values (7.2, 5.0) and shaken continuously (150 rpm) at 37°C . 2 mL of

the release solution was removed at predetermined time intervals. Then an equal amount of fresh PBS was added simultaneously to keep the total solution volume constant. A UV-vis absorption spectrometer determined the amount of PC B2 released from the release solution.

Characterization

The X-ray diffraction (XRD) analysis was carried out using an X-ray powder diffractometer (Bruker, D8). The morphologies of the PB NPs, MPB NPs, and HMPB NPs were characterized by a transmission electron microscope (TEM, JEM-200 CX) separately. Scanning electron microscopy (SEM) observation was carried out by field-emission SEM (Hitachi, SU-70). Specific surface area and corresponding pore-size distribution of MPB NPs and HMPB NPs were determined by using a Micromeritics ASAP 2460 (Micromeritics, Norcross, GA, USA). The UV-vis spectra were measured by a UV-vis spectrometer (Mapada, UV-1200). Hydrodynamic diameter (Dh) and Zeta potential of HMPB NPs were determined by dynamic light scattering (DLS) techniques using Malvern Zetasizer Nano-ZS 90 instrument.

Photothermal Performance of HMPB NPs

The photothermal performance of HMPB NPs was measured by an 808 nm NIR laser (MDL-H-808-5W, Changchun New Industry Optoelectronics Technology Co., Ltd., China). A digital thermometer was used to monitor the changes of temperature at different concentrations of HMPB NPs solutions in the cuvette. Next, the heating capacity of different power densities on the HMPB NPs solution was explored. To further evaluate the photothermal stability of the different materials, five cycles of NIR laser on/off tests were performed for PB NPs, MPB NPs, and HMPB NPs, respectively. The photothermal conversion efficiency and extinction coefficient of each material was calculated according to the Lin et al method.³⁷

Cellular Uptake

HeLa cells were plated in 6 well-plates (2×10^5 cells per well), and after cell adherence, the complete RPMI 1640 medium was discarded, and the cells were co-incubated with fresh complete RPMI 1640 medium containing FITC-OVA labeled HMPB NPs ($100 \mu\text{g mL}^{-1}$) for 8 h. Then the cells were washed three times with PBS, using inverted fluorescence microscopy (IFM) to observe whether these nanoparticles were endocytosed by cells.

In vitro Anti-Tumor Activity

HeLa cells (Shanghai Institutes of Life Sciences Cell Bank, Chinese Academy of Sciences) were plated in 96-well plates at a density of 5×10^3 cells per well, incubated with 5% CO_2 at 37°C for 24 hours. After the cell adherence, the medium was replaced and the cells were cultured with fresh complete RPMI 1640 medium, fresh complete RPMI 1640 medium containing PC B2 ($40 \mu\text{g mL}^{-1}$), fresh complete RPMI 1640 medium containing HMPB NPs ($100 \mu\text{g mL}^{-1}$), and fresh complete RPMI 1640 medium containing HMPB@PC B2 ($100 \mu\text{g mL}^{-1}$), respectively. After incubation, the cells were washed three times with PBS. In NIR treatment group, cells were exposed to an 808 nm NIR laser at a power density of 1 W cm^{-2} for 5 min and then incubated again at 37°C in 5% CO_2 for 24 h. Relative cell viability was determined by a standard MTT assay.

In vitro CLSM Observation and Flow Cytometry Analysis

HeLa cells (1×10^5 cells per dish) were plated on exclusive CLSM cell culture dishes and cultured for 24 hours. Then, the original culture medium was replaced with fresh complete RPMI 1640 medium, fresh complete RPMI 1640 medium containing HMPB NPs ($100 \mu\text{g mL}^{-1}$), and fresh complete RPMI 1640 medium containing HMPB@PC B2 ($100 \mu\text{g mL}^{-1}$), respectively, in which HMPB NPs and HMPB@PCB2 were co-incubated with HeLa cells for 12 h. Then, the cells were exposed to an 808 nm NIR laser at a power density of 2 W cm^{-2} for 5 min and incubated for another 12 h. The control group was incubated for 24 h. After that, the cells of all groups were stained with Calcein-AM ($5 \mu\text{L}$, 2 mM) and PI solution ($15 \mu\text{L}$, 1.5 mM), and live/dead cells were observed by CLSM.

For flow cytometry analysis, HeLa cells were plated in six-well plates (2×10^5 cells per plate) and treated as described previously. Cells were first digested with trypsin, then washed with PBS and collected by centrifugation, and

resuspended in binding buffer (100 μL). Subsequently, Annexin V-FITC (2.5 μL) and PI (5 μL) were added to the binding buffer separately with gentle mixing and stained for 15 min, protected from light. Finally, cell apoptosis was analyzed by flow cytometry.

In vivo Synergistic of PTT and CT

All animal experiments were performed according to protocols permitted by the Animal Care Committee of Xinjiang University (2022011401). BALB/c nude mice (female, 4 weeks old) were purchased from Beijing Vital River Experimental Animal Technology Co., Ltd. To obtain tumor-bearing animals, HeLa cells (5×10^6) were suspended in 100 μL PBS and subcutaneously injected in the forelimb of nude mice. The tumor-bearing mice were randomly divided into two groups: control and HMPB@PC B2+NIR ($n = 3$ mice per group). When the tumor volume reached about 100 mm^3 , the nude mice were intratumorally injected with PBS, and HMPB@PC B2 (1 mg mL^{-1} , 200 μL), respectively. After 12h, the groups of HMPB@PC B2 were exposed to 808 nm NIR laser (1 W cm^{-2}) for 5 min. Mice weight and tumor size were measured every other day.

At the end of the treatment, all mice were executed. The major organs such as heart, liver, spleen, lung, kidney and tumor were removed, fixed in 4% paraformaldehyde, embedded in a paraffin section. H&E staining analysis was conducted.

$$\text{Volume} = \frac{(\text{Tumor length}) \times (\text{Tumor width})^2}{2}$$

Results and Discussion

Design and Synthesis of HMPB NPs

HMPB NPs were synthesized via a hydrothermal method according to the literature, with some modifications.³⁴ As shown in [Figure 1A](#), briefly, face-centered cubic PB NPs was prepared via directly mixed PVP and $\text{K}_3[\text{Fe}(\text{CN})_6]$ under magnetic stirring. Then, the PB NPs were etched to obtain MPB NPs by 0.01 M HCl. Finally, the highly uniform dispersed HMPB NPs were obtained by further etching with 1M HCl ([Figure 1B–D](#)). In the whole etching process, the H^+ concentration in the center of the NPs was higher than the concentration on the surface, so the PB NPs was etched from the inside to the outside, which results in the formation of the interior cavity.³⁸ In the presence of low concentration of HCl (0.01 M), the solid structure of PB NPs transformed into the mesoporous structure and further transformed into the hollow mesoporous structure under high concentration of HCl (1M) etching. Transmission electron microscopy (TEM) demonstrated the whole process of transformation of solid PB NPs into mesoporous structures and finally into hollow mesoporous structures, which indicates the successful synthesis of HMPB NPs by controlled chemical etching ([Figure 1E–G](#)). Additionally, the results of X-ray diffraction of MPB NPs and HMPB NPs showed that the hollow mesoporous structure did not change its original crystallinity ([Figure S1](#)). Finally, DLS analysis showed that the average particle size of HMPB NPs was about 307.3 nm ([Figure S2A](#)) with zeta potential of about -15.9 mv ([Figure S2B](#)), resulting in well-dispersed in water. Besides, as-prepared HMPB NPs powder displayed excellent stability at room temperature and can be stored for more than half a year.

Photothermal Performance of HMPB NPs

The UV-visible absorption spectra acquired on PB NPs, MPB NPs, and HMPB NPs at different concentrations showed a broad, strong, and concentration-dependent absorption band from around 500 to 1000 nm ([Figure S3A–C](#)). It was shown that the absorption peak was red-shifted by structural modulation. Compared with PB NPs and MPB NPs, the absorbance of HMPB NPs at 808 nm was remarkably increased, from 0.66 (PB NPs) to 0.97 (HMPB NPs) ([Figure 2A](#)). The extinction coefficient of HMPB NPs at 808 nm was calculated to be $9.69 \text{ L g}^{-1} \text{ cm}^{-1}$ according to the Lambert-Beer law ([Figure S3F](#)), which is higher than PB NPs ($6.55 \text{ L g}^{-1} \text{ cm}^{-1}$) ([Figure S3D](#)) and MPB NPs ($8.37 \text{ L g}^{-1} \text{ cm}^{-1}$) ([Figure S3E](#)), indicating that HMPB NPs could have better photothermal conversion performance. Subsequently, to evaluate their photothermal conversion performance, PB NPs, MPB NPs, and HMPB NPs solutions were irradiated with an 808 nm NIR laser (1.5 W cm^{-2} , [Figure 2B](#)). The results showed that the temperature of HMPB NPs' (100 $\mu\text{g mL}^{-1}$) solution

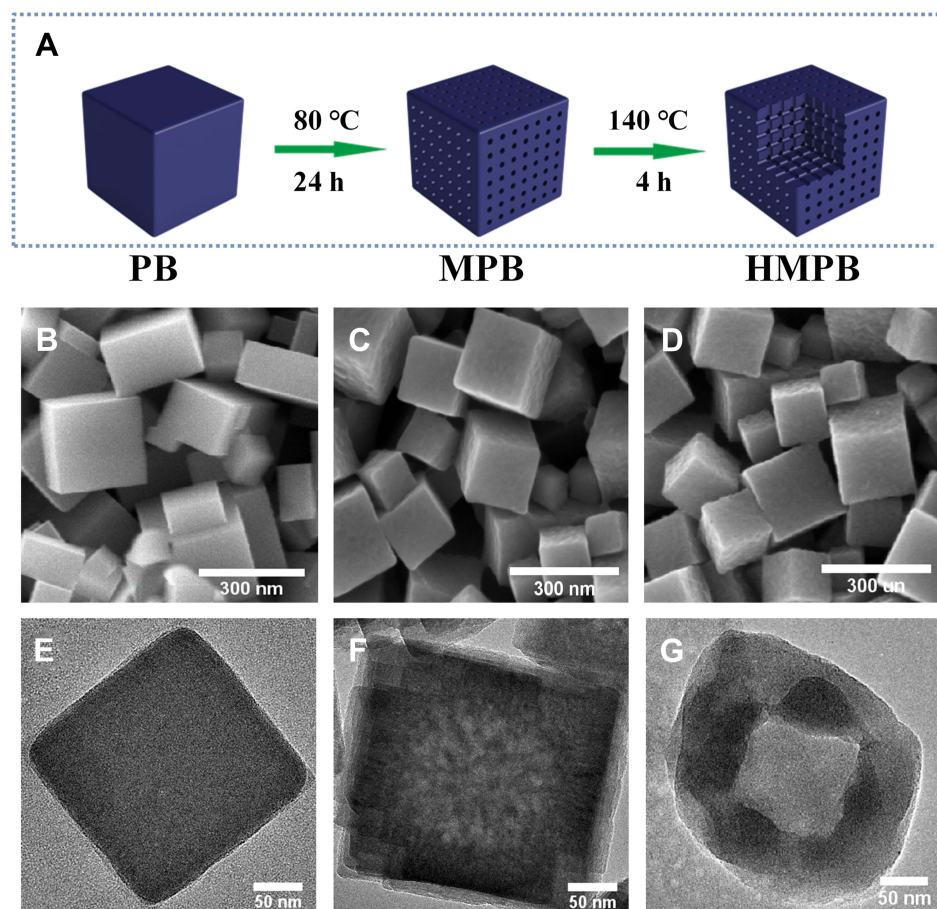


Figure 1 (A) Schematic illustration of synthetic procedure of HMPB NPs. The SEM images of (B) PB NPs, (C) MPB NPs, and (D) HMPB NPs. Scale bar 300 nm. The individual TEM images of (E) PB NPs, (F) MPB NPs, and (G) HMPB NPs. Scale bar 50 nm.

increased to 62.1°C within 10 min, which is significantly higher than PB NPs (55.0°C) and MPB NPs (58.3°C). This is consistent with the heating capacity of each nanomaterial under 1 W cm^{-2} NIR irradiation (Figure S4A), suggesting that HMPB NPs with excellent heating capacity due to their hollow mesoporous structure and higher molar extinction coefficient. Moreover, the heating capacity of HMPB NPs solutions under different power NIR light irradiation was explored (Figure S4B). With increasing power, the heating capacity of the same concentration of HMPB NPs solution became rapid, which indicates that the capacity of the HMPB NPs solutions depends on the laser power density. In parallel, the concentration-temperature dependence of HMPB NPs under NIR laser irradiation was also recorded (Figure S4C), manifesting the desirable photothermal performance of HMPB NPs. Furthermore, the photothermal stability of PB NPs, MPB NPs, and HMPB NPs were investigated for practical applications (Figures 2C and S5). We found no significant decay in the heating ability of HMPB NPs during five cycles (Figure 2C), which indicates that it could generate sufficient heat efficiently and consistently under NIR irradiation. Eventually, based on the calculated results of the time constant for heat transfer and maximum temperature, the photothermal conversion efficiency (η) of HMPB NPs at 808 nm was 30.13% (Figure 2D), which is significantly higher than that of PB NPs (27.47%) and MPB NPs (29.44%) (Figure S6A and B), indicating that HMPB NPs have better photothermal conversion efficiency. These results suggest that HMPB NPs can be used as effective NIR-mediated PTT compounds for tumor therapy.

Loading and Release Behavior of PC B2 in HMPB NPs

Encouraged by the unique structure and high specific surface area of HMPB NPs, its natural bioactive substances loading capacity was further investigated. First, N_2 adsorption-desorption isotherms of HMPB NPs were used to

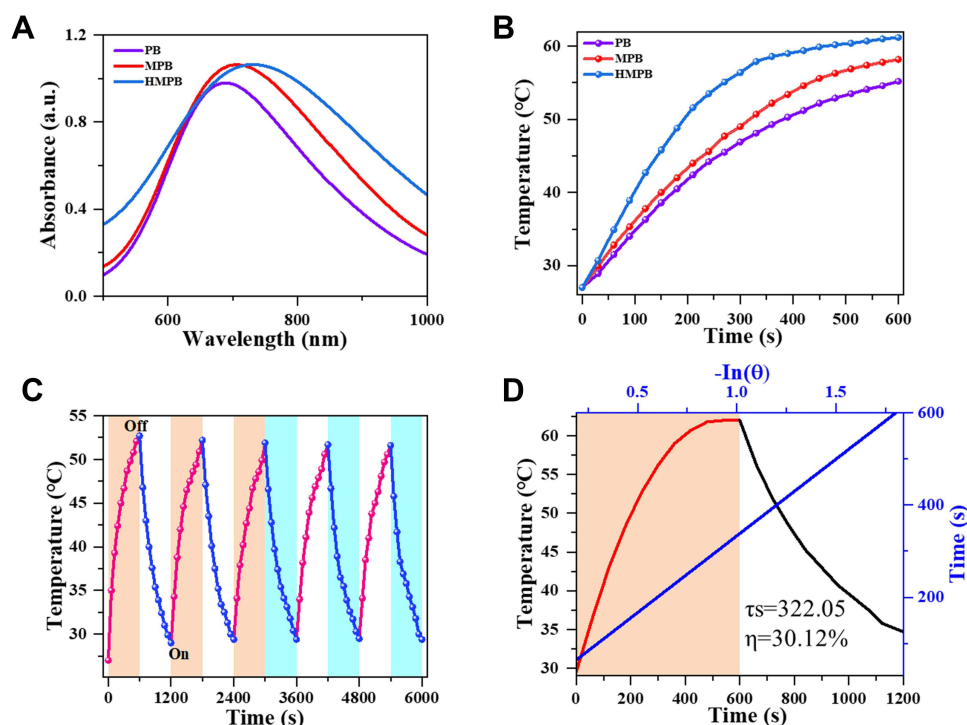


Figure 2 In vitro photothermal-conversion performance of different materials. The concentrations of PB NPs, MPB NPs and HMPB NPs were $100 \mu\text{g mL}^{-1}$. **(A)** UV-vis spectrum of PB NPs (purple), MPB NPs (red), and HMPB NPs (blue) at 808 nm. **(B)** Temperature-rise curves of PB NPs (purple), MPB NPs (red), and HMPB NPs (blue) within 10 min under irradiation of 808 nm NIR laser (1.5 W cm^{-2}). **(C)** Recycling heating curves of the solution containing HMPB NPs for five on/off cycles of the 808 nm NIR laser irradiation (1 W cm^{-2}). **(D)** Calculated photothermal-conversion efficiency of HMPB NPs at 808 nm. Red line: temperature change curves of the solution under 808 nm NIR laser irradiation for 10 min. Black line: cooling curve with NIR laser turned off. Blue line: time constant ($\tau_s=322.05$) for the heat transfer from the system obtained by applying the linear time data from the cooling period ($R^2=0.99869$).

evaluate the specific surface area and pore size of HMPB NPs. Typical Brunauer-Emmett-Teller (BET) indicated the wide internal pore size distribution (1.8 – 96.2 nm) and large specific surface area ($131.67 \text{ m}^2 \text{ g}^{-1}$) in HMPB NPs (Figures S7 and 3A), which have the potential to be an ideal carrier for bioactive substances. Herein, PC B2 was chosen as a cancer therapeutic agent and loaded into the HMPB NPs. As shown in the UV-visible absorption spectra and digital photographs of the inserted PC B2 solution before and after incubation with HMPB NPs (Figure 3B), the color of the loaded PC B2 solution became lighter, and the absorbance at 280 nm dropped dramatically, indicating that PC B2 was successfully loaded into the HMPB NPs. According to the calculation, the loading capacity of PC B2 can reach $329 \mu\text{g mg}^{-1}$ (Figures 3B and S9A–C), which is higher than that of $\text{CeO}_2@\text{SiO}_2\text{-PEG}$ nanoparticles ($294 \mu\text{g mg}^{-1}$), GO–N=N–GO/PVA composite nanohydrogels ($206.4 \mu\text{g mg}^{-1}$), dopamine conjugated nanographene oxide ($197.2 \mu\text{g mg}^{-1}$) and $\text{TiO}_2@\text{ZnO-GO}$ nanoparticles ($197.9 \mu\text{g mg}^{-1}$),^{39–42} indicating that HMPB NPs have an ultra-high loading capacity. More interestingly, the linkage of the $-\text{C}\equiv\text{N-Fe}$ group was unstable under the slightly acid environment. The degradation rate of HMPB in a slightly acidic environment (pH 5.0) was significantly higher (51.1%) than in a neutral environment (20.8%), implying the pH-responsive release behavior of HMPB NPs (Figures 3C, S8A and B). Furthermore, the cumulative release of PC B2 at different pH values (pH = 5.0 or 7.2) was investigated (Figures 3D and S10). The cumulative release of PC B2 was only 22.1% at pH 7.2 and increased sharply to 43.6% within 48 h when it dropped to 5.0, indicating that the release rate of PC B2 is higher in the slightly acidic environment. This is due to the decrease in pH that accelerates the degradation of HMPB NPs and promotes the release of PC B2. These results indicate that the ultra-high drug loading capacity and pH-responsive release behavior make HMPB@PC B2 become a promising excellent therapeutic agent.

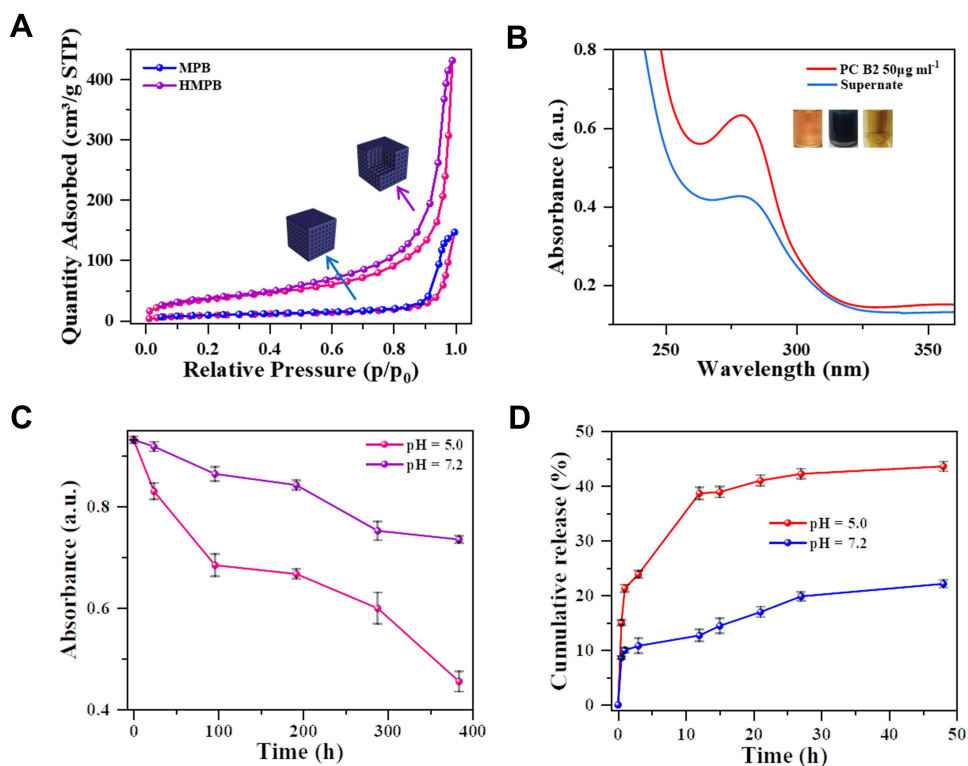


Figure 3 PC B2 loading and pH-responsive release. **(A)** N₂ adsorption-desorption isotherms of MPB NPs and HMPB NPs. **(B)** UV-visible absorption spectroscopy of PC B2 solutions before and after interaction with HMPB NPs (inset: the representative photos of PC B2 solution before (left) and after interaction with HMPB NPs (middle: before centrifugation, right: after centrifugation)). **(C)** Degradation curve of HMPB NPs at different pH values (5.0, 7.2). **(D)** In vitro release of PC B2 in HMPB@PC B2 at different pH values (5.0, 7.2).

In vitro Synergistic Therapeutic Efficacy

Inspired by excellent photothermal properties and high loading capacity of bioactive substances, then in vitro therapeutic efficiency of PC B2-loaded HMPB NPs was further investigated. Fluorescence microscopy (FM) was used to observe the uptake of HMPB NPs by HeLa cells ([Figure S11A](#)). The quantitative analysis of fluorescence images of cells showed that compared with FITC-OVA group, HMPB@FITC OVA group had the strongest green fluorescence intensity, suggesting that the HeLa cells could take-up HMPB NPs via endocytosis ([Figures S11B](#) and [C](#)). The relative viability of HeLa cells under HMPB alone or NIR laser irradiation alone had no significant difference compared with the control group, indicating the superior biocompatibility of HMPB NPs and the tolerance of HeLa cells to NIR laser. Further, the cytotoxicity of PC B2 was evaluated on 293T cells. When the concentration of PC B2 was as high as 640 μM, the cell viability remained over 90%, which indicated the excellent safety of PC B2 for normal tissues ([Figures 4A, B](#) and [S12B](#)). Whereas under the irradiation of NIR laser, as the concentration of HMPB NPs increased, the cell viability of HeLa decreased dramatically ([Figure S12A](#)). When the concentration of HMPB NPs was 100 μg mL⁻¹, the cell survival rate was only 47.9% ([Figure 4C](#)). These results suggest that HMPB NPs with superior biocompatibility could effectively kill HeLa cells under NIR laser. Then, the synergistic therapeutic effect of HMPB NPs with PC B2 was further evaluated. As illustrated in [Figure 4D](#), the synergistic effect of PTT and CT showed an enhanced cytotoxic compared with monotherapy. The therapeutic efficacy of the HMPB@PC B2 +NIR treatment group was 62.8%, which is higher than that of single CT (41.1%) and PTT (54.9%), suggesting that the synergistic strategy has a more obvious inhibitory effect on HeLa cells.

Consistent with MTT assay results, 55.3% cell apoptosis was detected in the HMPB@PC B2 + NIR treatment group, which is higher than the HMPB + NIR treatment group (46.7%) ([Figure 4E](#)), suggesting that the thermal energy generated under NIR irradiation and the release of PC B2 by HMPB@PC B2 greatly promote apoptosis thus inducing more extensive tumor cell death. Moreover, confocal laser scanning microscopy (CLSM) was used to visualize the live and dead HeLa cells in

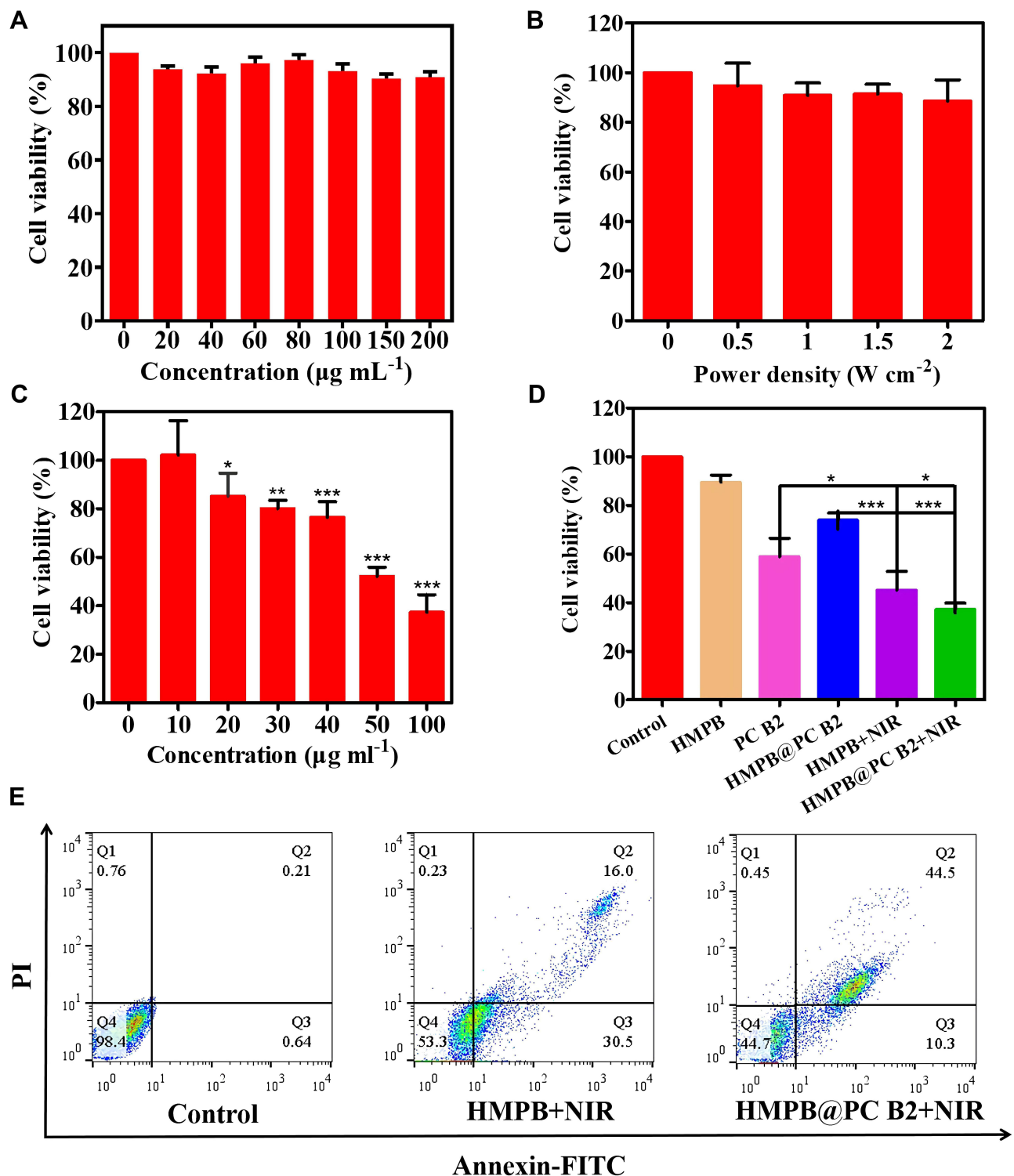


Figure 4 In vitro synergistic therapy efficacy. (A and B) Relative cell viabilities of the HeLa cells in various treatment groups: only HMPB NPs and only NIR laser. (C) Relative viability of HeLa cells under NIR laser irradiation with different concentrations of HMPB NPs. (D) Relative cell viabilities of HeLa cells in various treatment groups (HMPB, HMPB@PC B2: 100 $\mu\text{g mL}^{-1}$; PC B2: 40 $\mu\text{g mL}^{-1}$). (E) Flow cytometry analysis of HeLa cells' apoptosis in various treatment groups. (* $p < 0.05$; ** $p < 0.01$; and *** $p < 0.005$).

different treatment groups. The Calcein-AM and PI fluorescence intensity of each group in Figure 5A corresponds to Figure 5C. And the results of the fluorescence quantitative analysis of the HMPB+NIR group and HMPB@PC B2 group are shown in Figure 5B, which show that there was a significant difference in the PI/Calcein-AM fluorescence intensity ratio

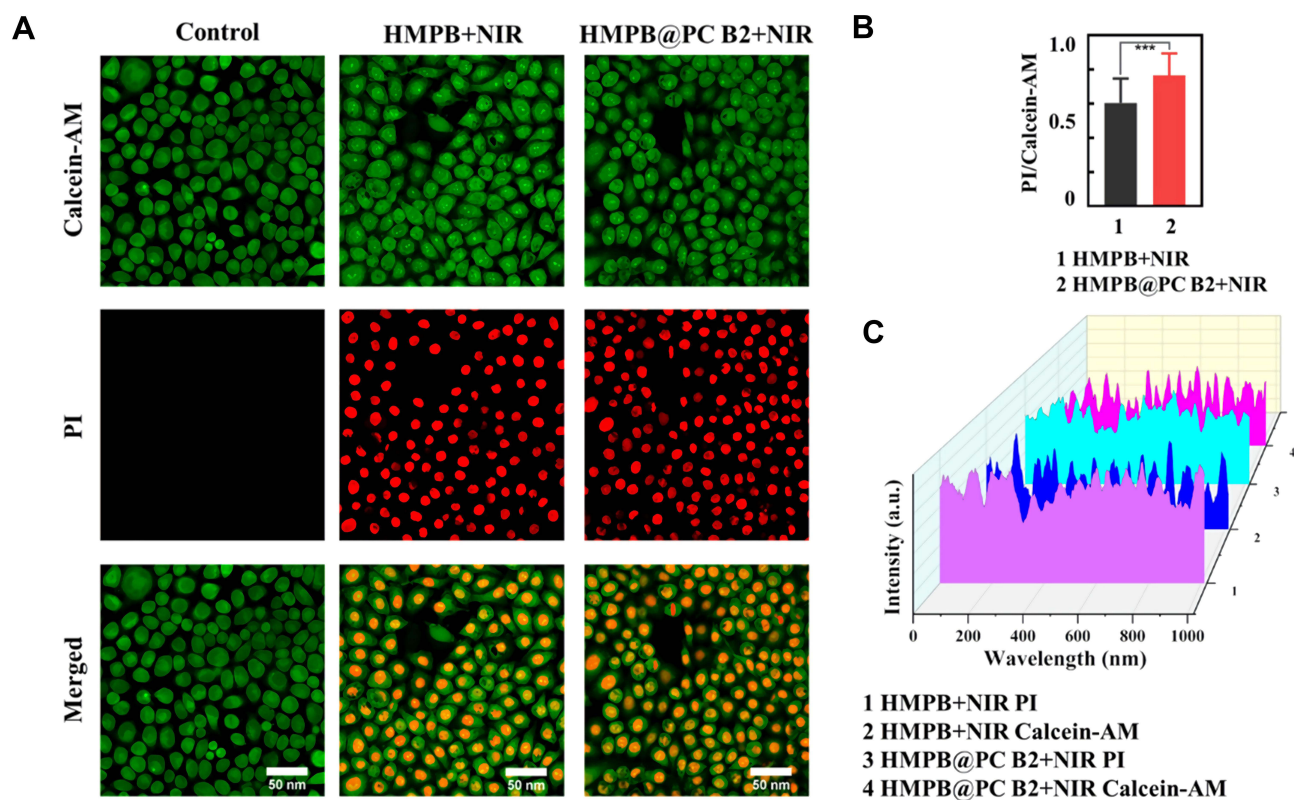


Figure 5 (A) CLSM images of HeLa cells stained by Calcein-AM/PI in treatment groups. (B) Quantitative analysis of the relative fluorescence intensity in the two treatment groups. (C) Waterfall plot of the relative fluorescence intensity in the two treatment groups. (***) $p < 0.005$.

between the two groups, indicating more cell death in the HMPB@PC B2+NIR group. These results imply that combination treatment obviously promotes treatment efficacy.

In vivo Excellent Therapeutic Efficacy

Given the excellent therapeutic efficacy and biocompatibility of HMPB@PC B2 in vitro, its anti-tumor efficacy was further evaluated in HeLa-bearing Balb/c nude mice. Firstly, the photothermal performance of HMPB@PC B2 in vivo was measured (Figure 6A). The HeLa-tumor-bearing mice were intratumorally injected with PBS and HMPB@PC B2, respectively. Then, the maximum temperature at the tumor site increased from 30.2°C to 51.5°C under 808 nm (1 W cm⁻²) NIR laser. In contrast, the temperature of the tumor tissue in the control group did not show significant fluctuations (Figure 6B). The outstanding photothermal performance of HMPB@PC B2 in vivo is sufficient for tumor therapy. After the treatment, representative tumor photographs of different treatment groups demonstrated the excellent anti-tumor efficacy of HMPB@PC B2 (Figure 6C and D). The tumor of mice in the HMPB@PC B2+NIR group were significantly smaller compared with the control group. And tumor weight and tumor volume changes are shown in Figure 6E and F. Obviously, HMPB@PC B2+NIR treatment reduced the tumor volume after 14 days' treatment by about 65% due to the elevated temperature and the release of PC B2. This result demonstrates the superior efficacy of PTT and CT in tumor therapy. More surprisingly, no significant difference in body weight was observed in all groups of mice during treatment (Figure 6G), indicating that HMPB@PC B2 has satisfactory biocompatibility and biosafety in vivo.

At the end of the whole treatment period, major organs and tumors of all mice were collected for histological analysis. The H&E staining results showed that the HMPB@PC B2 + NIR treatment group had significant damage to the tumor tissue, as evidenced by cellular crinkling and nuclear chromatin condensation and fragmentation (Figure S13). Nevertheless, no obvious abnormalities were found in the major organ sections of the group, indicating that this treatment method did not cause significant inflammation and damage to the major organs. At the same time, the blood index of nude mice was measured and showed negligible changes in the HMPB@PC B2 group compared with the

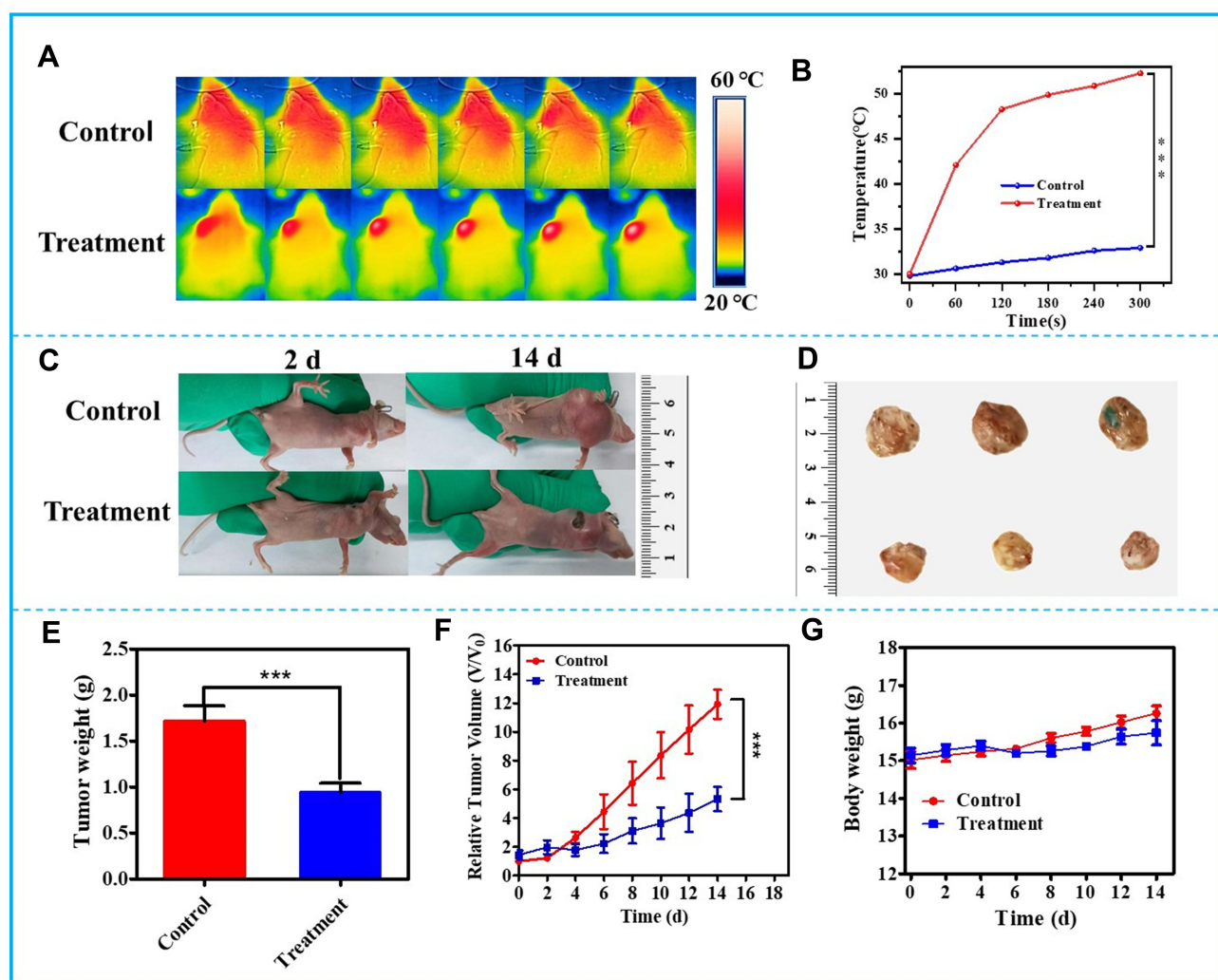


Figure 6 In vivo therapeutic efficacy of HMPB@PC B2. (A) In vitro thermographic images of tumor-bearing mice after injection of PBS, HMPB@PC B2 with 808 nm NIR laser irradiation, and (B) the corresponding temperature changes at the tumor site of mice under 808 nm NIR laser irradiation (1W cm^{-2}) in different groups. (C) Digital images of the nude mice before and after treatment. (D) Digital images of tumors dissected from each group at the end of treatments. (E) Tumor weight changes in various treatment groups. (F) Relative tumor volume changes and (G) body weight changes in various treatment groups within 14 days. (** $p < 0.005$).

control group (Figures S14 and S15). Therefore, this treatment strategy is proven to have excellent safety without significant systemic toxicity.

Conclusion

In this work, biocompatible HMPB@PC B2 bio-nanocomposites were constructed by encapsulating PC B2 into HMPB NPs with a hollow mesoporous structure. Under the slightly acidic TME, the biodegradation of HMPB NPs resulted in the sustained release of PC B2 in vivo to produce a powerful CT effect. More interestingly, based on the inherent photothermal conversion property of HMPB NPs, the anti-tumor activity of HMPB@PC B2 could be further enhanced by the higher temperature generated via NIR radiation. The in vitro and in vivo experiments demonstrated that the PTT and CT provided excellent cancer therapy efficiency without toxicity. Thus, the constructed HMPB@PC B2 represents a promising anti-cancer therapeutic nanoplatform, enabling in situ release of bioactive substances for efficient multimodal synergistic therapy.

Acknowledgments

This work was supported by the National Natural Science Foundation of China (No: 31960496), Natural Science Foundation of Xinjiang (No. 2019D01C054), Tianshan Innovation Team Project in Xinjiang Autonomous Region (2020D14022), Tianshan Youth Foundation of Xinjiang (2019Q066).

Disclosure

The authors report no conflicts of interest in this work.

References

1. Feng J, Wu L, Ji J, et al. PKM2 is the target of proanthocyanidin B2 during the inhibition of hepatocellular carcinoma. *J Exp Clin Canc Res*. 2019;1:1–15. doi:10.1186/s13046-019-1194-z
2. Firdous A, Sharmila G, Balakrishnan S, et al. Quercetin, a natural dietary flavonoid, acts as a chemopreventive agent against prostate cancer in an in vivo model by inhibiting the EGFR signaling pathway. *Food Funct*. 2014;5(10):2632–2645. doi:10.1039/c4fo00255e
3. Zhang H, Tsao R. Dietary polyphenols, oxidative stress and antioxidant and anti-inflammatory effects. *Curr Opin Food Sci*. 2016;8:33–42. doi:10.1016/j.cofs.2016.02.002
4. Cheah KY, Howarth GS, Bindon KA, Kennedy JA, Bastian S. Low molecular weight procyanidins from grape seeds enhance the impact of 5-Fluorouracil chemotherapy on Caco-2 human colon cancer cells. *PLoS One*. 2014;9(6):e98921. doi:10.1371/journal.pone.0098921
5. Huang S, Yang N, Liu Y, et al. Grape seed proanthocyanidins inhibit colon cancer-induced angiogenesis through suppressing the expression of VEGF and Ang1. *Int J Mol Med*. 2012;30(6):1410–1416. doi:10.3892/ijmm.2012.1147
6. Kumar R, Deep G, Wempe MF, Agarwal R, Agarwal C. Procyanidin B2 3,3'-di-o-gallate inhibits endothelial cells growth and motility by targeting VEGFR2 and integrin signaling pathways. *Curr Cancer Drug Targets*. 2015;15(1):14–26. doi:10.2174/1568009614666141229102254
7. Maqsoodlou A, Assadpour E, Mohebodini H, Jafari SM. The influence of nano delivery systems on the antioxidant activity of natural bioactive compounds. *Crit Rev Food Sci*. 2020;1:1–24. doi:10.1080/10408398.2020.1863907
8. Feng F, Li R, Zhang Q, et al. Preparation of reduction-triggered degradable microcapsules for intracellular delivery of anti-cancer drug and gene. *Polymer*. 2014;55(1):110–118. doi:10.1016/j.polymer.2013.11.035
9. Kang L, Gao Z, Huang W, Jin M, Wang Q. Nanocarrier-mediated co-delivery of chemotherapeutic drugs and gene agents for cancer treatment. *Acta Pharm Sin B*. 2015;5(3):169–175. doi:10.1016/j.apsb.2015.03.001
10. Céspedes MV, Unzueta U, Álamo P, et al. Cancer-specific uptake of a liganded protein nanocarrier targeting aggressive CXCR⁴⁺ colorectal cancer models. *Nanomed-Nanotechnol*. 2016;7:1987–1996. doi:10.1016/j.nano.2016.04.003
11. Jyothi NVN, Prasanna PM, Sakarkar SN, Prabha KS, Ramaiah PS, Srawan G. Microencapsulation techniques, factors influencing encapsulation efficiency. *J Microencapsul*. 2010;3:187–197. doi:10.1079/BJN20061848
12. Kurokawa C, Fujiwara K, Morita M, et al. DNA cytoskeleton for stabilizing artificial cells. *P Natl Acad Sci USA*. 2017;28:7228–7233. doi:10.1073/pnas.1702208114
13. Peng S, Zou L, Zhou W, Liu W, Liu C, McClements DJ. Encapsulation of lipophilic polyphenols into nanoliposomes using the pH-driven method: advantages and disadvantages. *J Agr Food Chem*. 2019;67(26):7506–7511. doi:10.1021/acs.jafc.9b01602
14. Chen Q, Wang X, Wang C, Feng L, Li Y, Liu Z. Drug-induced self-assembly of modified albumins as nano-theranostics for tumor-targeted combination therapy. *ACS Nano*. 2015;9:5223–5233. doi:10.1021/acs.nano.5b00640
15. Yang G, Chen Q, Wen D, et al. A therapeutic microneedle patch made from hair-derived keratin for promoting hair regrowth. *ACS Nano*. 2019;13(4):4354–4360. doi:10.1021/acs.nano.8b09573
16. Kojima C, Nishisaka E, Suehiro T, et al. The synthesis and evaluation of polymer prodrug/collagen hybrid gels for delivery into metastatic cancer cells. *Nanomed-Nanotechnol*. 2013;6:767–775. doi:10.1016/j.nano.2013.01.004
17. Andrieu J, Re F, Russo L, Nicotra F. Phage-displayed peptides targeting specific tissues and organs. *J Drug Target*. 2019;27:555–565. doi:10.1080/1061186X.2018.1531419
18. Pena-Francesch A, Jung H, Hickner MA, Tyagi M, Allen BD, Demirel MC. Programmable proton conduction in stretchable and self-healing proteins. *Chem Mater*. 2018;30(3):898–905. doi:10.1021/acs.chemmater.7b04574
19. Yang Q, Cao J, Yang F, et al. Amyloid-like aggregates of bovine serum albumin for extraction of gold from ores and electronic waste. *Chem Eng J*. 2021;416:129066. doi:10.1016/j.cej.2021.129066
20. Teasdale I, Wilfert S, Nischang I, Brüggemann O. Multifunctional and biodegradable polyphosphazenes for use as macromolecular anti-cancer drug carriers. *Polym Chem*. 2011;2(4):828–834. doi:10.1039/C0PY00321B
21. Paul A, Eun CJ, Song JM. Cytotoxicity mechanism of non-viral carriers polyethylenimine and poly-L-lysine using real time high-content cellular assay. *Polymer*. 2014;55(20):5178–5188. doi:10.1016/j.polymer.2014.08.043
22. Lian HY, Hu M, Liu CH, Yamauchi Y, Wu KCW. Highly biocompatible, hollow coordination polymer nanoparticles as cisplatin carriers for efficient intracellular drug delivery. *Chem Commun*. 2012;48(42):5151–5153. doi:10.1039/c2cc31708g
23. Zhang W, Hu S, Yin JJ, et al. Prussian blue nanoparticles as multienzyme mimetics and reactive oxygen species scavengers. *J Am Chem Soc*. 2016;138(18):5860–5865. doi:10.1021/jacs.5b12070
24. Perrier M, Gallud A, Ayadi A, et al. Investigation of cyano-bridged coordination nanoparticles Gd³⁺/[Fe(CN)₆]³⁻/D-mannitol as T1-weighted MRI contrast agents. *Nanoscale*. 2015;7(28):11899–11903. doi:10.1039/C5NR01557J
25. Cai X, Jia X, Gao W, et al. A versatile nanotheranostic agent for efficient dual-mode imaging guided synergistic chemo-thermal tumor therapy. *Adv Funct Mater*. 2015;25(17):2520–2529. doi:10.1002/adfm.201403991
26. Hu M, Furukawa S, Ohtani R, et al. Synthesis of Prussian blue nanoparticles with a hollow interior by controlled chemical etching. *Angew Chem Int Ed*. 2012;4:984–988. doi:10.1002/anie.201105190

27. Jia X, Cai X, Chen Y, et al. Perfluoropentane-encapsulated hollow mesoporous Prussian blue nanocubes for activated ultrasound imaging and photothermal therapy of cancer. *ACS Appl Mater Inter.* 2015;7(8):4579–4588. doi:10.1021/am507443p
28. Niu C, Zou B, Wang Y, Chen L, Zheng H, Zhou S. The template-assisted synthesis of polypyrrole hollow microspheres with a double-shelled structure. *Chem Commun.* 2015;51(24):5009–5012. doi:10.1039/c4cc10445e
29. Liang G, Xu J, Wang X. Synthesis and characterization of organometallic coordination polymer nanoshells of Prussian blue using miniemulsion periphery polymerization (MEPP). *J Am Chem Soc.* 2009;131(15):5378–5379. doi:10.1021/ja900516a
30. Roy X, Hui JKH, Rabnawaz M, Liu G, MacLachlan MJ. Prussian blue nanocontainers: selectively permeable hollow metal-organic capsules from block ionomer emulsion-induced assembly. *J Am Chem Soc.* 2011;133(22):8420–8423. doi:10.1021/ja2016075
31. Yang R, Hou M, Gao Y, et al. Indocyanine green-modified hollow mesoporous Prussian blue nanoparticles loading doxorubicin for fluorescence-guided tri-modal combination therapy of cancer. *Nanoscale.* 2019;11(12):5717–5731. doi:10.1039/c8nr10430a
32. Fu G, Liu W, Feng S, Yue X. Prussian blue nanoparticles operate as a new generation of photothermal ablation agents for cancer therapy. *Chem Commun.* 2012;48(94):11567–11569. doi:10.1039/c2cc36456e
33. Jing L, Liang X, Deng Z, et al. Prussian blue coated gold nanoparticles for simultaneous photoacoustic/CT bimodal imaging and photothermal ablation of cancer. *Biomaterials.* 2014;35(22):5814–5821. doi:10.1016/j.biomaterials.2014.04.005
34. Cai X, Gao W, Ma M, et al. Prussian blue-based core-shell hollow-structured mesoporous nanoparticle as a smart theranostic agent with ultrahigh pH-responsive longitudinal relaxivity. *Adv Mater.* 2015;27(41):6382–6389. doi:10.1002/adma.201503381
35. Borkowska M, Siek M, Kolygina DV, et al. Targeted crystallization of mixed-charge nanoparticles in lysosomes induces selective death of cancer cells. *Nat Nanotechnol.* 2020;15(4):331–341. doi:10.1038/s41565-020-0643-3
36. Jiang W, Zhang H, Wu J, et al. CuS@MOF-based well-designed quercetin delivery system for chemo-photothermal therapy. *ACS Appl Mater Interfaces.* 2018;10(40):34513–34523. doi:10.1021/acsami.8b13487
37. Lin H, Gao S, Dai C, Chen Y, Shi J. A two-dimensional biodegradable niobium carbide (MXene) for photothermal tumor eradication in NIR-I and NIR-II biowindows. *J Am Chem Soc.* 2017;139(45):16235–16247. doi:10.1021/jacs.7b07818
38. Zhang Q, Zhang T, Ge J, Yin Y. Permeable silica shell through surface-protected etching. *Nano Lett.* 2008;8(9):2867–2871. doi:10.1021/nl8016187
39. Chen Z, Xu L, Gao X, et al. A multifunctional CeO₂@ SiO₂-PEG nanoparticle carrier for delivery of food-derived proanthocyanidin and curcumin as an effective antioxidant, neuroprotective and anti-cancer agent. *Food Res Int.* 2020;137:109674. doi:10.1016/j.foodres.2020.109674
40. Hou L, Shi YY, Jiang GX, et al. Smart nanocomposite hydrogels based on azo crosslinked graphene oxide for oral colon-specific drug delivery. *Nanotechnology.* 2016;27(31):315105. doi:10.1088/0957-4484/27/31/315105
41. Masoudipour E, Kashanian S, Maleki N. A targeted drug delivery system based on dopamine functionalized nano graphene oxide. *Chem Phys Lett.* 2017;668:56–63. doi:10.1016/j.cplett.2016.12.019
42. Zamani M, Rostami M, Aghajanzadeh M, Manjili HK, Rostamizadeh K, Danafar H. Mesoporous titanium dioxide@ zinc oxide-graphene oxide nanocarriers for colon-specific drug delivery. *J Mater Sci.* 2018;53(3):1634–1645. doi:10.1007/s10853-017-1673-6

International Journal of Nanomedicine

Dovepress

Publish your work in this journal

The International Journal of Nanomedicine is an international, peer-reviewed journal focusing on the application of nanotechnology in diagnostics, therapeutics, and drug delivery systems throughout the biomedical field. This journal is indexed on PubMed Central, MedLine, CAS, SciSearch[®], Current Contents[®]/Clinical Medicine, Journal Citation Reports/Science Edition, EMBase, Scopus and the Elsevier Bibliographic databases. The manuscript management system is completely online and includes a very quick and fair peer-review system, which is all easy to use. Visit <http://www.dovepress.com/testimonials.php> to read real quotes from published authors.

Submit your manuscript here: <https://www.dovepress.com/international-journal-of-nanomedicine-journal>